

# Chapter 1. Introduction

## *1.1 Synthesis of MicroElectroMechanical Systems (MEMS)*

MEMS design involves the use of different device topologies in a creative way and sizing these topologies to meet the requirements on performance. There are essentially two steps: one, to develop an interconnection of springs, masses and actuators to perform the desired function and second, to assign appropriate values to these components so that the performance of the device is satisfactory. In general, there are a number of design variables (we have identified 15 for the microresonator) and complex trade-offs between different performance specifications. Therefore, it is difficult to design MEMS by hand. Currently, MEMS design is done with the aid of an equations-based spreadsheet or finite element analysis (FEA) to evaluate the designs. This requires many iterations by the designer with different values assigned to the device dimensions or other design variables in each iteration. The design procedure is, therefore, time-consuming. FEA cannot evaluate all the performance metrics of interest, or may be restricted to certain specific domains (like only mechanical analyses or only electrostatic analyses). The performance specifications and the design variables themselves are not restricted to discrete values and can take on a continuum of values. This makes pre-compiled cell libraries (like digital cell libraries) ineffective as a good design aid. In designing complex/arrayed MEMS which make use of a number of similar devices, it is tedious to individually design each cell.

A layout synthesis tool generates device layouts directly from high-level specifications. This involves appropriate assignment of values to the design variables followed by device-layout generation. Prior work on layout synthesis has addressed the parameterized layout generation of microresonators [1][2]. Optimal design techniques have been reported for simple MEMS geometries [3]. However, there is no full-fledged synthesis tool for MEMS.

The goal of this work is to develop the prototype of a synthesis tool using the microresonator as a vehicle. The tool will relieve the designer of the task of sizing the design, thus, allowing him

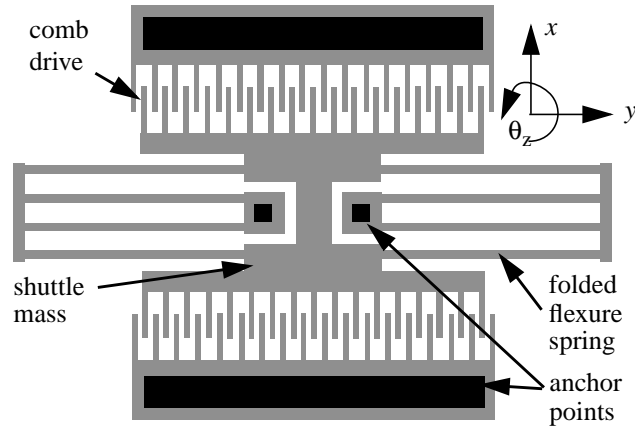


**FIGURE 1. Layout of the lateral folded-flexure comb drive microresonator. The black areas are the places where the 2  $\mu\text{m}$  polysilicon structure is anchored to the bottom layer. The rest of the structure is suspended 2  $\mu\text{m}$  above the bottom layer.**

to concentrate on system-level design issues and on innovative device topologies. Different parts of the work detailed in this thesis have been published over the past two years [4][5][6][7][8].

### *1.2 Folded-Flexure comb drive Microresonator*

The folded-flexure electrostatic comb drive micromechanical resonator shown in Figure 1 was first introduced by Tang [9]. This device has been well-researched and is commonly used for MEMS process characterization. The microresonator consists of a movable central shuttle mass which is suspended by folded-flexure springs on either side. The other ends of the folded-flexure springs are fixed to the lower layer. The microresonator can be thought of, as a spring-mass-damper system, the damping being provided by the air below and above the movable part. By applying a voltage across the fixed and movable comb fingers, an electrostatic force is produced which sets the mass into motion in the x-direction. The microresonator has been used in building filters, oscillators [10] and in resonant positioning systems [11].

A simplified sequence of MUMPS [12], used to fabricate this device is shown in Figure 2. Layers of silicon nitride and polysilicon are deposited on a silicon substrate. Following this a 2  $\mu\text{m}$ -thick phosphosilicate glass (PSG) layer (which serves as the sacrificial layer) is deposited. Cuts are made in the PSG layer where the structural layer requires to contact the bottom polysilicon layer. A 2  $\mu\text{m}$ -thick polysilicon layer is deposited on top of this PSG layer and patterned to the

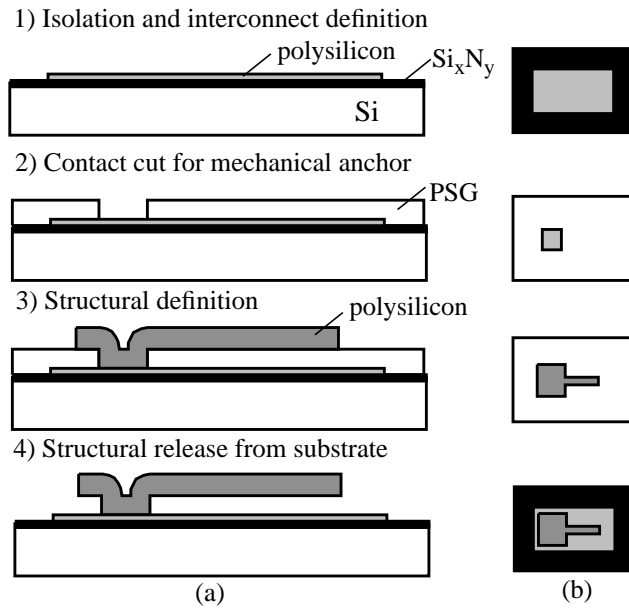


**FIGURE 2. Abbreviated process flow for MCNC's Multi-User MEMS Process service (MUMPS). (a) Cross-sectional view. (b) Top view (layout)**

desired shape. The underlying PSG is then released by wet etching using hydrofluoric acid (HF) leaving the structural polysilicon suspended 2  $\mu\text{m}$  above the bottom layer and fixed to the bottom layer at the regions where the contact cuts were made in the PSG layer.

### *1.3 Report Outline*

In Chapter 2, the equations describing the behavior of the microresonator are derived. Following this, the synthesis approach is described in Chapter 3. In Chapter 4, the synthesis results are evaluated by comparing the predicted behavior to finite element analyses and experimental measurements. Finally, in Chapter 5, the work done is summarized and future directions for synthesis are suggested.

## Chapter 2. Lumped Element Modeling

### 2.1 Introduction

In order to evaluate the performance of a design we need models for the device behavior. The general approach we have taken in modeling the resonator is to represent distributed elements like plate masses and folded-flexure springs by a single lumped element having equivalent *effective* properties (like mass, stiffness, etc.) The entire device can then be regarded as an interconnection of these lumped elements and the device behavior can be easily expressed in terms of the properties of these lumped elements. This is analogous to modeling a transmission line as a simple  $\pi$ -connected R-L-C network with *effective* values for the R, L and C (not just the total resistance of the line substituted for R).

We have modeled the microresonator as a spring-mass-damper system in the x-direction. Physics-based models for the effective spring stiffness of the folded-flexure suspensions, the effective masses of the shuttle mass, comb drives and the folded-flexure, and the viscous air damping are used in the synthesis tool. The microresonator structure can also have other modes of vibration. These modes are modeled as spring-mass systems as described in Section 2.2.

The models for the electrostatic comb drive force and the electrostatic instability force/torque (which may arise due to an offset of the movable comb fingers away from their equilibrium central position) are described in Section 2.3.

### 2.2 Modeling the Oscillation Modes of the Microresonator

The preferred direction of motion of the microresonator is the x-direction. However, the microresonator structure can vibrate in other modes. We have modeled eight modes of vibration of the microresonator. These modes are the three translation modes along x, y and z, three rotational modes about x, y and z, and oscillation modes due the movement of the folded-flexure beams and the comb drive.

Each oscillation mode is described by a lumped second-order equation of motion. For any generalized displacement  $\zeta$ , we can write:

$$F_{e,\zeta} = m_\zeta \ddot{\zeta} + B_\zeta \dot{\zeta} + k_\zeta \zeta \quad (1)$$

where  $F_{e,\zeta}$  is the external force (in the  $x$ -mode this force is generated by the comb drives),  $m_\zeta$  is the effective mass,  $B_\zeta$  is the damping coefficient, and  $k_\zeta$  is the spring constant. Now, for example, the  $x$ -mode frequency is given by  $\omega_x = 2\pi f_x = \sqrt{k_x/m_x}$ . The other modes are modeled similarly.

Linear equations for the spring constants are derived using energy methods [13]. A force (or moment) is applied to the free end(s) of the spring in the direction of interest, and the displacement is calculated symbolically (as a function of the design variables and the applied force). In these calculations different boundary conditions are applied for the different modes of deformation of the spring.

When forces (moments) are applied at the end-points of the flexure, the total energy of deformation,  $U$ , is calculated as:

$$U = \sum_{beam\ i=1}^N \int_0^{L_i} \left( \frac{M_i(\xi)^2}{2EI_i} + \frac{T_i(\xi)^2}{2GJ_i} \right) d\xi \quad (2)$$

where,  $L_i$  is the length of the  $i$ 'th beam in the flexure,  $M_i$  is the bending moment transmitted through beam  $i$ ,  $E$  is the Young's modulus of the material of the beam (polysilicon, in our case) and  $I_i$  is the moment of inertia of beam  $i$ , about the relevant axis,  $T_i$  is the torsion transmitted through beam  $i$ ,  $G$  is the shear modulus,  $J_i$  is the torsion constant of beam  $i$ , and  $\xi$  is the variable along the length of the beam. The bending moment and the torsion is a linear function of the forces and moments applied to the end-points of the flexure. The displacement of an end-point of the flexure in any direction  $\zeta$  is given as:

$$\delta\zeta = \frac{\partial U}{\partial F_\zeta} \quad (3)$$

where,  $F_\zeta$  is the force applied in that direction at that end-point [14]. Similarly, angular displacements can be related to applied moments.

Our aim here is to obtain the displacement in the direction of interest as a function of the applied force in that direction. Applying the boundary conditions, we obtain a set of linear equations in terms of the applied forces and moments and the unknown displacement. Solving the set of equations yields a linear relationship between the displacement and applied force in the direction of interest [13]. The constant of proportionality gives the spring constant as a function of the physical dimensions of the flexure.

The effect of spring mass on resonance frequency is incorporated in effective masses for each lateral mode. Effective mass for each mode of interest is calculated by normalizing the total maximum kinetic energy of the spring by the maximum shuttle velocity,  $v_{max}$ .

$$m_{eff} = \sum_{beam\ i=1}^N \frac{m_i}{L_i} \int_0^{L_i} \left( \frac{v_i(\xi)}{v_{max}} \right)^2 d\xi \quad (4)$$

where  $m_i$  and  $L_i$  are the mass and length of the  $i$ 'th beam in the flexure. Analytic expressions for velocities,  $v_i$ , along the flexure's beams are approximated from static deformation shapes, and are found from the spring constant derivations.

### 2.2.1 Models for $x$ -translation Mode

The spring constant of the folded-flexure in the  $x$ -direction is [13]:

$$k_x = \frac{2Et w_b^3}{L_b^3} \frac{L_t^2 + 14\alpha L_t L_b + 36\alpha^2 L_b^2}{4L_t^2 + 41\alpha L_t L_b + 36\alpha^2 L_b^2} \quad (5)$$

where  $E$  is the Young's modulus of polysilicon,  $t$  is the polysilicon thickness, and  $\alpha = (w_t/w_b)^3$ .

The geometrical layout parameters  $L_t$ ,  $L_b$ ,  $w_t$  and  $w_b$  are as shown in Figure 3.

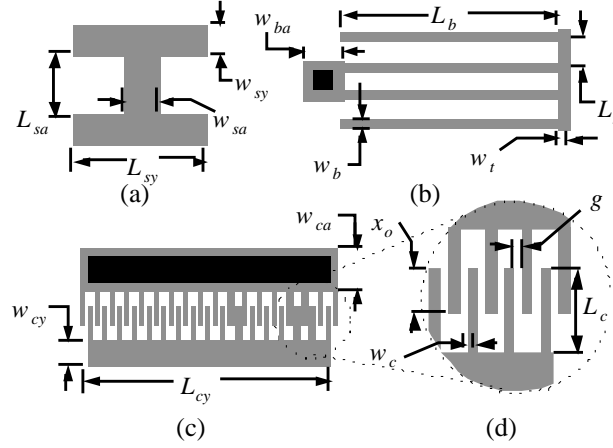


**FIGURE 3. Dimensions of the microresonator elements. (a) shuttle mass, (b) folded-flexure, (c) comb drive with N movable ‘rotor’ fingers, (d) close-up view of comb fingers.**

In order to calculate the effective mass accurately, it is not only necessary to take into account the velocities of the beams in the folded-flexure in the x-direction, but also the velocities of the truss beams in the y-direction. With this, the net effective mass of the microresonator in the x-direction ( $m_x$ ) can be written as:

$$m_x = m_{shuttle} + m_{t, eff} + m_{b, eff} \quad (6)$$

$$m_{b, eff} = \frac{m_{beams}}{140} \frac{832L_t^4 + 16121\alpha L_t^3 L_b + 92706\alpha^2 L_t^2 L_b^2 + 138348\alpha^3 L_t L_b^3 + 62208\alpha^4 L_b^4}{(4L_t^2 + 41\alpha L_t L_b + 36\alpha^2 L_b^2)^2} \quad (7)$$

$$m_{t, eff} = \frac{m_{truss}}{280} (57L_t^6 + 1020\alpha L_t^5 L_b + 4644\alpha^2 L_t^4 L_b^2 + 1120L_t^4 L_b^2 + 17920\alpha L_t^3 L_b^3 + 91840\alpha^2 L_t^2 L_b^4 + 161280\alpha^3 L_t L_b^5 + 90720\alpha^4 L_b^6) / [L_b^2(4L_t^2 + 41\alpha L_t L_b + 36\alpha^2 L_b^2)^2] \quad (8)$$

where  $m_{shuttle}$  is the shuttle mass,  $m_{t, eff}$  is the effective mass of all truss sections,  $m_{b, eff}$  is the effective mass of all the long beams,  $m_{truss}$  is the total mass of all truss sections,  $m_{beams}$  is the total mass of all the long beams.

Viscous air damping dominates the energy dissipation mechanisms in microresonators at atmospheric pressure. The total damping force in the x-direction is mainly composed of the forces due to Couette flow below the resonator, Stokes flow above the resonator, and air flow in the gap between comb fingers. The expression for the damping coefficient is [15]:

$$B_x = \mu \left[ (A_s + 0.5A_t + 0.5A_b) \left( \frac{1}{d} + \frac{1}{\delta} \right) + \frac{A_c}{g} \right] \quad (9)$$

where  $\mu$  is the viscosity of air,  $d$  is the fixed spacer gap between the ground plane and the bottom surface of the comb fingers,  $\delta$  is the penetration depth of airflow above the structure,  $g$  is the gap between comb fingers, and  $A_s$ ,  $A_t$ ,  $A_b$ , and  $A_c$  are layout areas for the shuttle, truss beams, flexure beams, and comb finger sidewalls, respectively. It has been suggested [15] that, for calculating the viscous damping force, small cross-section elements (like comb fingers) should be weighted thrice as much as large plate masses to take into account edge and finite-size effects. Instead of weighting the damping force on different elements differently, the same phenomena are modeled in this work by extending each device dimension by  $4 \mu\text{m}$ . The damping factors of the modes of vibrations other than the x-direction are not modeled.

### 2.2.2 Models for the y-translation Mode

The spring stiffness of the folded-flexure in y-direction is [13]:

$$k_{y, flexure} = \frac{2Etw_t^3}{L_t^3} \frac{8L_t^2 + 8\alpha L_t L_b + \alpha^2 L_b^2}{4L_t^2 + 10\alpha L_t L_b + 5\alpha^2 L_b^2} \quad (10)$$

However, this model does not take into account the compression of the beams. The spring stiffness due to compression alone is given by Hooke's law as:

$$k_{y, beamcomp} = \frac{2Etw_b}{L_b} \quad (11)$$

The effective spring constant in the y-direction is given as a combination of the two springs:

$$k_{y, eff} = \frac{k_{y, flexure} \cdot k_{y, beamcomp}}{k_{y, flexure} + k_{y, beamcomp}} \quad (12)$$

The effective mass in the y-direction is given as:

$$m_y = m_{shuttle} + m_{t, yeff} + m_{b, yeff} \quad (13)$$



$$m_{b,yeff} = m_{beams} \left( \frac{1}{2} + \left( (3L_b^4 \alpha^2 (2L_t + \alpha L_b)^2) / 14L_t^2 (4L_t^2 + 10\alpha L_t L_b + 5\alpha^2 L_b^2)^2 \right) \right) \quad (14)$$

$$m_{t,yeff} = \frac{m_{truss}}{1120} \frac{(3328L_t^4 + 16064\alpha L_t^3 L_b + 26868\alpha^2 L_t^2 L_b^2 + 17828\alpha^3 L_t L_b^3 + 4077\alpha^4 L_b^4)}{[(4L_t^2 + 10\alpha L_t L_b + 5\alpha^2 L_b^2)^2]} \quad (15)$$

where  $m_{t,yeff}$  is the effective mass of all truss sections,  $m_{b,yeff}$  is the effective mass of all the long beams in the y-direction of motion.

### 2.2.3 Models for the z-translation Mode

The spring stiffness in the z-translation mode is derived in [13] and is not listed here for the sake of brevity. The effective mass in the z-direction is:

$$m_z = m_{shuttle} + \frac{1}{4}m_{truss} + \frac{12}{35}m_{beams} \quad (16)$$

### 2.2.4 Models for the Rotation-about-z Mode

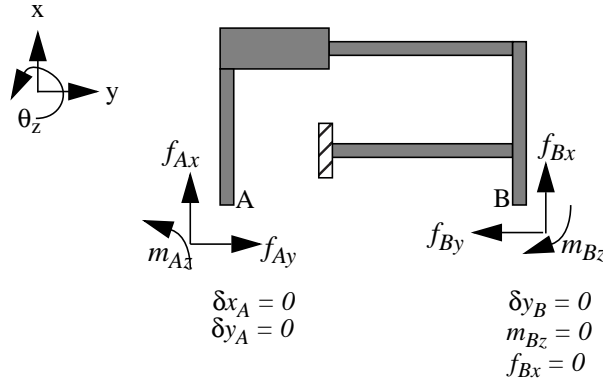


**FIGURE 4. Forces and moments applied on the free ends of a half folded-flexure (with y-axis of symmetry) for in-plane rotation. Boundary conditions to calculate the spring constant in the rotation-about-z mode are also shown.**

To calculate the spring stiffness of the folded-flexure in the rotation-about-z mode, a moment  $m_{Az}$  is applied to the half folded-flexure, as shown in Figure 4 [16]. This moment produces reaction forces  $f_{Ax}, f_{Ay}, f_{Bx}, f_{By}$  and a reaction moment  $m_{Bz}$ . From symmetry considerations,  $m_{Bz}$  and  $f_{Bx}$  have to be zero. This leaves us with 3 unknowns,  $f_{Ax}, f_{Ay}$  and  $f_{By}$ . In this mode the flexure move-

ment is such that the boundary conditions are as follows. The point A does not translate in the x or y directions. Therefore,  $\delta x_A = 0$  and  $\delta y_A = 0$ . The point B does not translate along the y-axis. Therefore,  $\delta y_B = 0$ . These boundary conditions are summarized in Table I. Beam compression effects are found to be significant for this mode. Therefore, for calculation of the spring stiffness, an additional energy term is included in the right hand side of (2), which takes into account the energy due to axial compression in the folded-flexure beams. The spring stiffness is then calculated as explained previously (using (3)). The expression for the spring constant is extremely long and is not listed here in full detail. A first-order approximation when  $\alpha \gg 1$ ,  $L_b \gg L_t$  and beam compression effects are neglected is:

$$k_{\theta_z, flexure} = \frac{2Et w_t^3}{3L_t^3} L_x^2 \quad (17)$$

where,  $L_x$  is the distance of the center of the outer folded-flexure beam from the center of the shuttle mass along the x-axis. It is seen that  $k_{\theta_z, flexure}$  is very sensitive to variations in the width and the length of the truss-beam.

The moment of inertia about the z-axis,  $I_z$ , is calculated as if the entire structure rotates by the same angle, as :

$$I_z = \sum_{rectangle\ i=1}^N \left( m_i \frac{(w_i^2 L_i + L_i^2 w_i)}{12} + m_i r_i^2 \right) \quad (18)$$

where,  $m_i$  is the mass of the  $i$ 'th rectangular block,  $w_i$  and  $L_i$  are the width and the length respectively, of that face of the  $i$ 'th block which is normal to the z-axis (in general, the face normal to the axis of rotation),  $r_i$  is the distance of the center of mass of the block from the z-axis and the microresonator is made up of  $N$  blocks.

The straight-forward calculation explained above results in an over-estimation of the moment of inertia, since portions of the folded-flexure closer to the anchor do not rotate as much as the

shuttle mass rotates. Therefore, the predicted resonant frequency for this mode will be lower than the actual frequency. This is acceptable for the synthesis, since we are only interested in keeping the frequency of this mode well-separated from the frequency of the x-mode.

### 2.2.5 Models for the Rotation-about-x Mode

A moment  $m_{Ax}$  is applied to the half folded-flexure, as shown in Figure 5. The relations are summarized in the first row of Table I. The spring stiffness is then calculated as explained previ-

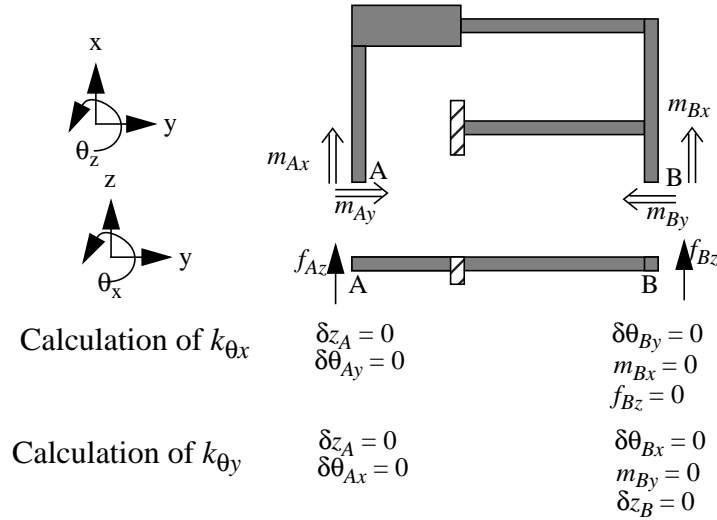


FIGURE 5. Forces and moments applied on the free ends of a half folded-flexure (with y-axis of symmetry). Boundary conditions to calculate the spring constants in the two out-of-plane rotational modes are also shown.

Table I Calculation of spring-constants for the rotational modes

Axis of Rotation	Applied Moment	Reaction Forces/ Moments	Symmetry Considerations	Unknowns	Boundary Conditions
x	$m_{Ax}$	$f_{Az}$ , $m_{Ay}$ $f_{Bz}$ , $m_{Bx}$ $m_{By}$	$m_{Bx}=0$ $f_{Bz}=0$	$f_{Az}$ , $m_{Ay}$ $m_{By}$	$\delta z_A = 0$ $\delta \theta_{Ay} = 0$ $\delta \theta_{By} = 0$
y	$m_{Ay}$	$f_{Az}$ , $m_{Ax}$ $f_{Bz}$ , $m_{Bx}$ $m_{By}$	$m_{By}=0$ ;	$f_{Az}$ , $m_{Ay}$ $f_{Bz}$ , $m_{By}$	$\delta z_A = 0$ $\delta \theta_{Ax} = 0$ $\delta z_B = 0$ $\delta \theta_{Bx} = 0$
z	$m_{Az}$	$f_{Ax}$ , $f_{Ay}$ $f_{Bx}$ , $f_{By}$ $m_{Bz}$	$m_{Bz}=0$ $f_{Bx}=0$	$f_{Ax}$ , $f_{Ay}$ , $f_{By}$	$\delta x_A = 0$ $\delta y_A = 0$ $\delta y_B = 0$

ously (using (2) and (3)). If the central shuttle yoke is assumed to be highly rigid, an approximate expression for the spring stiffness is:

$$k_{\theta_x, flexure} = \frac{Et^3 w_t}{3L_b^3} \left[ \frac{2\beta L_b^3 + 3L_b^2 L_t + 6\beta L_b^2 L_y + 6L_b L_t L_y + 6\beta L_b L_y^2 + 3L_t L_y^2}{\beta L_b + 2L_t} \right] \quad (19)$$

where,  $L_y = L_{sy}/2$  and  $\beta = \frac{GJ_t}{EI_{x,b}}$ ,  $I_{x,b}$  is the moment of inertia of a long folded-flexure beam

about the x-axis and  $J_t$  is the torsion constant for a truss beam. The expression for the torsion constant for a rectangular beam is listed in [13].

The moment of inertia about the x axis is calculated as if the entire structure rotates by the same angle, similar to the calculation of the moment of inertia about the z-axis.

### 2.2.6 Models for the Rotation-about-y Mode

To calculate the spring stiffness of the folded-flexure in the rotation-about-y mode, a moment  $m_{Ay}$  is applied to the half folded-flexure, as shown in Figure 5. The relations are once again summarized in Table I and the spring stiffness is calculated via (2) and (3). The expression for the spring constant is extremely long and is not listed here. If the truss is assumed to be very stiff (i.e., very wide), and the length of the beams is much greater than the length of the truss sections, (i.e.,  $L_b \gg L_t$ ) the dominant terms in the expression reduce to:

$$k_{\theta_y, flexure} = \frac{Et^3 w_b}{6L_b^3} \cdot \frac{\gamma^2 L_b^4 + 6\gamma L_b^2 L_t^2 - 12\gamma L_b^2 L_t L_x + 15\gamma L_b^2 L_x^2 + 9L_t^2 L_x^2}{\gamma L_b^2 + 3L_t^2} \quad (20)$$

where,  $\gamma = \frac{GJ_b}{EI_{x,b}}$ ,  $J_b$  is the torsion constant for the folded-flexure beams.

The moment of inertia about the y-axis is calculated similar to the other two rotation modes.

### 2.2.7 Models for the Folded-flexure Beam Mode

Two vibration modes are observed due to the movement of the folded-flexure beams, one in which the two springs on either side are in phase (symmetric) and the other mode in which the two

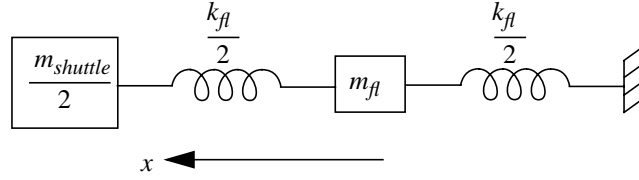


**FIGURE 6. One-dimensional model for determining resonant frequency of the flexure modes, where  $m_{shuttle}$  is the shuttle mass,  $k_{fl}$  is the flexure spring constant, and  $m_{fl}$  is the flexure effective mass. Only half of the resonator is modeled, taking advantage of symmetry.**

springs are  $180^\circ$  out-of-phase (anti-symmetric). The frequencies of these two modes are usually very close. We have modeled the symmetric mode with the one-dimensional half-resonator system shown in Figure 6 [16]. The flexure behavior is lumped into an effective mass,  $m_{fl}$ , and a flexure spring,  $k_{fl}$ , which is split into an anchored component and a component connected to the shuttle mass. The second modal frequency of this system is

$$\omega_{fl} = 2\pi f_{fl} = \sqrt{\frac{k_{fl}}{m_{fl}} \left( 1 + \frac{m_{fl}}{2m_{shuttle}} + \left( \frac{m_{fl}}{2m_{shuttle}} \right)^2 \right)} \quad (21)$$

where, assuming an infinitely stiff truss, the flexure effective mass is

$$m_{fl} = \frac{m_{truss}}{2} + \frac{6}{35}m_{beams} \quad (22)$$

In this vibration mode, the truss beams oscillate with the maximum amplitude. Therefore, their masses appear directly in (22) (Note:  $m_{truss}$  is the mass of all the truss beams in *two* folded flexure springs), while the contribution of the beams is calculated using (4).

The flexure spring constant is obtained by treating each beam as a guided-end beam [13] and summing the individual spring constants.

$$k_{fl} = 4Et \left( \frac{w_b}{L_b} \right)^3 \quad (23)$$

### 2.2.8 Models for the Comb Drive Oscillation Mode

The comb drive is stiff in the in-plane directions since it is usually more wide than thick. However, it is typically not very stiff in the z-direction. Therefore, there will be a vibration mode

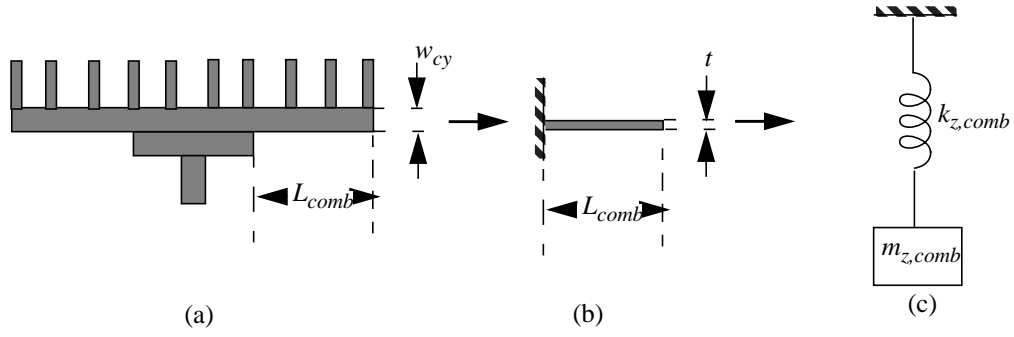


**FIGURE 7. Modeling the vibration mode of the comb drive. (a) comb drive (b) Equivalent cantilever beam (c) Spring-mass model**

due to motion of the comb drive in the z-direction. In this mode, the portion of the comb drive extending along the y-direction, outside the shuttle mass, oscillates in the z-direction, while, the rest of the structure, including the central portion of the comb drive which is attached to the shuttle mass, is almost stationary. This mode is also modeled as a spring-mass system. The spring stiffness of the comb drive in the z-direction is equal to that of a cantilever beam whose length is equal to  $L_{comb}$ , shown in Figure 7.

$$k_{z,comb} = \frac{E w_{cy} t^3}{4 L_{comb}^3} \quad (24)$$

where,  $L_{comb} = (1/2) (L_{cy} - L_{sy})$ .

The effective mass of the comb drive is calculated using (4). The velocity is zero at the end of the comb drive which is near the shuttle and is maximum at the position of the outer-most finger. The comb drive mode shape is assumed to be cubic. The effective mass is then given by:

$$m_{z,comb} = \frac{23}{140} m_{comb} \quad (25)$$

where,  $m_{comb}$  is the mass of the portion of the comb drive of length  $L_{comb}$ .

## 2.3 Electrostatic Force Models

### 2.3.1 Comb Drive Force in $x$

General analytic equations for the lateral comb drive force,  $F_x$ , as a function of comb finger width,  $w_c$ , air gap between comb fingers,  $g$ , structure thickness,  $t$ , and sacrificial spacer thickness,  $d$ , are derived in [17]. For the special case of equal comb finger width, gap, thickness, and spacing above the substrate ( $w_c = g = t = d$ ), each comb drive generates a force that is proportional to the square of the voltage,  $V$ , applied across the comb fingers.

$$F_x \cong 1.12\epsilon_o N \frac{t}{g} V^2 \quad (26)$$

where  $\epsilon_o$  is the permittivity of air,  $N$  is the number of fingers in the movable comb drive,  $V$  is the instantaneous voltage applied across the comb drive.

### 2.3.2 Electrostatic Instability Models

If the comb fingers are not perfectly centered, a  $y$ -directed electrostatic force is also present. In the absence of restraining springs, this force will result in snapping of the movable comb fingers and the stationary comb fingers. Assuming a small perturbation  $\delta y$  in the  $y$ -direction, the destabilizing force,  $F_{e,y}$ , is proportional to displacement such that  $F_{e,y} = k_{e,y} \delta y$ , where  $k_{e,y}$  is an ‘electrical negative spring constant.’

$$k_{e,y} \approx 2\epsilon_o N V^2 x_o \frac{t}{g^3} \quad (27)$$

If there is a small rotation  $\delta\theta$ , about the  $z$ -axis, a destabilizing electrostatic torque,  $\tau_{e,\theta} = k_{e,\theta} \delta\theta$  is generated by the comb drive. The rotational spring constant is found by realizing that the destabilizing force acts through a moment arm,  $X_c$ , on the center of the resonator, giving [16]:

$$k_{e,\theta} = k_{e,y} X_c^2 \approx 2\epsilon_o N V^2 x_o \frac{t}{g^3} X_c^2 \quad (28)$$

where  $X_c = 0.5 L_{sa} + w_{cy} + L_c - 0.5 x_o$  (Refer to Figure 3 and Table II for definitions of the geometric design variables).

#### 2.4 Summary

The microresonator has been modeled in detail and equations predicting the modes of the microresonator as functions of the geometrical parameters have been derived. Models have also been derived for the comb drive electrostatic forces. These lumped-element models are used by the synthesis tool for rapidly evaluating candidate designs.



## Chapter 3. Synthesis Methodology

The synthesis methodology involves the identification of all the degrees of freedom and the constraints on the design problem. The development of the synthesis tool is initiated by identifying the design variables that capture the degrees of freedom in the design space. Following this, we define the design space by limiting each design variable to lie between a maximum and minimum. Constraints, which the design variables should satisfy in order for the design to be acceptable, are then formulated. Different objective functions such as *minimize area*, are implemented in order to drive the synthesis towards preferred types of designs (smaller designs, in the case of the *minimize area* objective function). The synthesis is achieved through an optimization algorithm which seeks to minimize a cost function and simultaneously satisfy the constraints.

### 3.1 Design Variables

Fifteen design variables are identified for the microresonator. The design variables are listed in Table II and shown in Figure 3. These include 13 geometrical parameters (shown in Figure 3), the number of fingers in the comb drive,  $N$ , and the effective voltage,  $V$ , applied to the comb drive. When the resonator is operated with a dc voltage  $V_{dc}$  applied to the shuttle, and a sinusoidal volt-

**Table II Design and style variables for the microresonator. Upper and lower bounds are in units of  $\mu\text{m}$  except  $N$  and  $V$ .**

DESIGN VARIABLES							
Var.	Description	Min	Max	Var.	Description	Min	Max
$L_b$	length of flexure beam	2	400	$w_{cy}$	width of comb yoke	10	400
$w_b$	width of flexure beam	2	20	$L_{cy}$	length of comb yoke	2	700
$L_t$	length of truss beam	2	400	$L_c$	length of comb fingers	8	400
$w_t$	width of truss beam	2	20	$w_c$	width of comb fingers	2	20
$L_{sy}$	length of shuttle yoke	2	400	$g$	gap between comb fingers	2	20
$w_{sy}$	width of shuttle yoke	10	400	$x_o$	comb finger overlap	4	400
$w_{sa}$	width of shuttle axle	10	400				
$N$	number of rotor comb fingers	1	100	$V$	voltage amplitude	1 V	50V
STYLE VARIABLES							
$w_{ba}$	width of beam anchors	11	11	$w_{ca}$	width of stator comb anchors	14	14

age source with amplitude  $V_{ac}$  applied to only one of the actuators, we can simplify the applied voltage as an effective sinusoidal voltage with amplitude  $V = \sqrt{2V_{ac}V_{dc}}$ . Technology-driven design rules set minimum beam widths and minimum spaces between structures. Maximum beam lengths are constrained to 400  $\mu\text{m}$  to avoid problems with undesirable curling due to stress gradients in the structural film and possible sticking and breakage during the wet release etch [18]. Maximum width of beams is constrained to 20  $\mu\text{m}$  by the limited undercut of PSG to release the structures. The shuttle axle, the shuttle yoke and the comb yoke are at least 10  $\mu\text{m}$  wide so that, they are relatively more rigid than folded-flexure beams. The comb yoke is allowed to extend up to 700  $\mu\text{m}$ , to fill up the entire flexure length allowed for the resonator, even if the comb fingers occupy only a fraction of a length of the comb yoke.

Geometric “style” variables are necessary to completely define the layout, but do not affect the resonator behavior. Therefore, they are not part of the set of design variables. They usually define the stationary parts of the device, such as the anchors for the stationary comb fingers and the folded-flexure beams. While setting these variables the design rules should be followed. These variables are set to fixed values and include the width of the anchor supports,  $w_{ba}$  and  $w_{ca}$ , the offset of attachment points of the flexure beams to the anchor edge, and the overlap around anchor cuts.

### *3.2 Constraints*

The constraints can be classified into two kinds: geometrical constraints which are directly related to the physical dimensions of the microresonator and functional constraints which are related to the behavior of the microresonator.

### 3.2.1 Geometrical Constraints

The geometric constraints illustrated in Figure 8 are necessary to ensure a functional resonator. The constraints are detailed in Table III. The resonator width and length must not exceed an arbitrary fixed size, set at  $700\ \mu\text{m}$  in the example presented. Depending on the design, either the flexure or the comb drive actuator may define the overall resonator length. Therefore, both constraints need to be simultaneously satisfied. The actuator length constraint is linear (an alternative non-linear form of the constraint would have been  $(2N + 1)w_c + 2Ng$ ). Choosing a linearized version of any constraint aids in the efficiency of the optimization-based synthesis. With the introduction a design variable,  $L_{cy}$ , for the length of the comb finger yoke there is an extra degree of freedom, which allows the comb drive yoke to be longer than the minimum length required to accommodate all the comb fingers. However, there is a possibility that the comb drive length may not be sufficient to hold all the fingers. To avoid this there is a comb-fill constraint:  $(2N + 1)w_c + 2Ng \leq L_{cy}$ .

Gaps between the comb fingers and between the shuttle and beam anchor must allow the shuttle to move freely and must accommodate the maximum possible stroke. The maximum

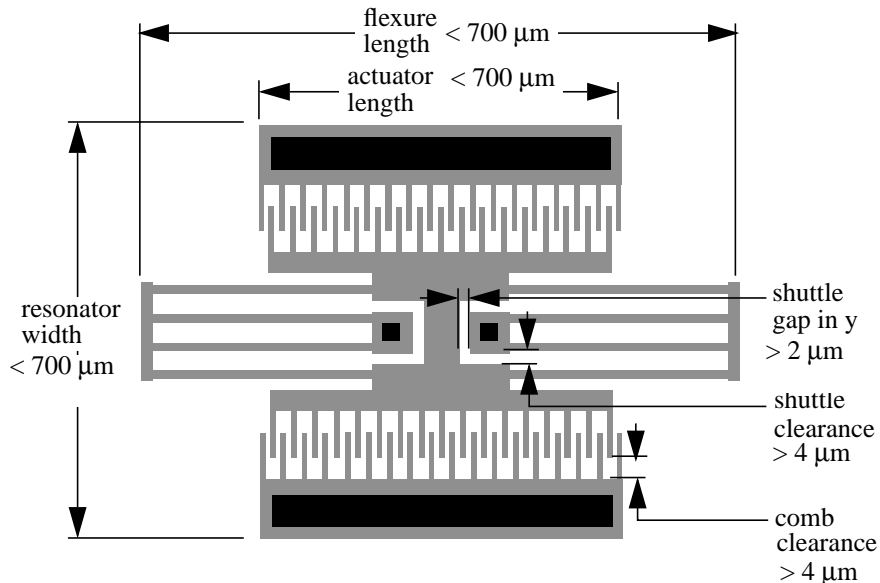


**FIGURE 8. Geometric constraints.** These constraints limit the overall size of the microresonator and also prevent the moving parts from colliding into the fixed parts of the microresonator.

**Table III Geometric Constraints**

Constraint Description	Expression	min [ $\mu\text{m}$ ]	max [ $\mu\text{m}$ ]
actuator length I	$L_{cy} + 2g + 2w_c$	0	700
comb-fill	$(2N+1)w_c + 2Ng - L_{cy}$	700	0
flexure length	$L_{sy} + 2L_b + 2w_t$	0	700
total resonator width	$3L_t + w_{sy} + 4L_c - 2x_o + 2w_{cy} + 2w_{ca}$	0	700
comb clearance during motion	$L_c - (x_o + x_{disp})$	4	200
minimum comb overlap	$x_o - x_{disp}$	4	200
shuttle clearance during motion	$L_t - x_{disp} - (w_{sy} + w_b)/2$	4	200
shuttle gap in y	$(L_{sy} - 2w_{ba} - w_{sa})/2$	2	200

expected displacement of the shuttle mass will be at resonance, and is encoded in the motion limit constraints using  $x_{disp}$ . First, we ensure that the comb fingers do not crash into each other at the maximum displacement. Next, we constrain the minimum comb overlap at the maximum displacement, to maintain linearity of the comb drive actuation. We also constrain the resonator geometry to ensure an adequate shuttle clearance during movement of the shuttle. Finally, a shuttle gap constraint is defined to encode the technology-driven design rule for gaps between moving and anchored parts.

### 3.2.2 Functional Constraints

Constraints on the design specifications are assigned realistic values for synthesizing a valid resonator for use as a characterization structure. Alternative constraint values can be readily assigned in the implementation.

An essential specification is resonant frequency of the lowest (preferred) mode. A valid layout must have a resonant frequency within 1% of the desired value ( $f_{spec}$ ). Resonant frequencies of the other in-plane modes,  $f_{\theta}$ ,  $f_{\theta_z}$  and  $f_y$ , (collectively represented by  $f_i$  in Table IV) must be at least three times greater than  $f_x$  to decouple the modes adequately. For the out-of-plane modes of vibration, the quality factor is expected to be much lower than for the in-plane modes, since squeeze-

film damping between the microresonator and the bottom layer will dominate over viscous air damping due to lateral motion. Therefore, even if these modes are closer to the x-mode than the in-plane modes, their oscillations will be more damped. Additionally, it is very difficult to achieve the *factor of three* in mode separation for the out-of-plane modes. Hence, the out-of-plane modes  $f_z$ ,  $f_{\theta_x}$ , and  $f_{\theta_y}$  (collectively represented by  $f_o$  in Table IV) are constrained to be at least twice greater than  $f_x$ . For stability, the restoring force of the spring in the y direction must be three times greater than the destabilizing electrostatic force from the comb drive (*i.e.*,  $3k_{e,y} < k_y$ ). A similar stability constraint must hold for the rotational mode.

Assuming the system is underdamped, the displacement amplitude at resonance is  $x_{disp} = Q_x F_x / k_x$ , where  $F_x \propto NV^2$  is the comb drive force,  $Q_x = \sqrt{m_x k_x / B_x^2}$  is the quality factor, and  $B_x$  is the damping coefficient. To enable easy visual confirmation of resonance the displacement amplitude is constrained to be at least 2  $\mu\text{m}$ . A quality factor constraint,  $Q_x \geq 5$ , is also implemented to ensure underdamped resonant operation.

Some of the lumped-parameter macromodels were derived based on simplifying assumptions. For example, in the y direction, we assume that the shuttle compliance will never dominate the flexure stiffness. We encode this assumption as a design constraint by ensuring that  $k_{y,axle} > 10k_y$ . In the x direction, we assume that the flexure stiffness will be linear. To encode this concern, we use an *ad hoc* value of 10 for the ratio of beam length to the maximum displacement. In other words, the upper limit on the deflection of the beam is 10% of the beam length.

Finite residual stress in mechanical polysilicon films can cause released fixed-fixed suspensions to break in tension or buckle under compression. Polysilicon can be deposited either compressive or tensile, depending on deposition conditions. In the MUMPs process, residual stress is always compressive, having a nominal value of -10 MPa and worst-case value of -20 MPa.

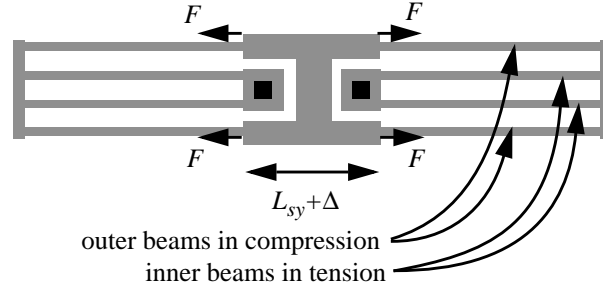


**FIGURE 9. Effect of compressive residual stress on the folded-flexure suspension. The expansion of the central shuttle mass pushes the outer beams. If the stress due to this is greater than a critical value, the outer beams will buckle.**

Beams in the folded flexure are free to expand outward to relieve residual axial stress. However, as shown in Figure 9, the central shuttle also expands an amount  $\Delta$  due to residual stress, creating additional axial stress in the outer beams and tension in the inner beams. A first-order value of the critical buckling length,  $L_{cr}$ , for the folded-flexure is given by the Euler column formula,  $L_{cr} = \pi w \sqrt{2I_b / 3\Delta}$ , where  $2L_b < L_{cr}$  to ensure no buckling, and  $w$  corresponds to the minimum of  $w_b$  and  $t$ .

A summary of the functional constraints on the design specifications is given in Table IV.

**Table IV Functional Constraints**

Constraint Description	Expression	min	max
resonant frequency	$f_x/f_{spec}$	0.99	1.01
stroke at resonance	$x_{disp}$	2 $\mu\text{m}$	100 $\mu\text{m}$
quality factor in x	$Q_x$	5	$10^5$
y-axis stability	$k_{e,y}/k_y$	0	1/3
$\theta_z$ stability	$k_{e,\theta_z}/k_{\theta_z}$	0	1/3
in-plane mode separation	$f_x/f_i$	0	1/3
out-of-plane mode separation	$f_x/f_o$	0	1/2
$k_y$ accuracy	$k_y/k_{y,axle}$	0	1/10
$k_x$ accuracy	$x_{disp}/L_b$	0	1/10
buckling	$L_b/L_{cr}$	0	1/2

### 3.3 Synthesis Formulation

Synthesis of the microresonator will result in one of two possible outcomes. Several designs may satisfy the above constraints, or no designs may meet the constraints (null design space). Our

synthesis approach is to select the design that minimizes an objective function and therefore, may be considered optimal. The synthesized result depends very strongly on the choice of objective function.

Generally, smaller area devices are preferred for cost reduction. Smaller operating voltages are also preferred for integrated devices. Therefore, three objective functions to be minimized are implemented: total active area, amplitude of the comb drive voltage, and the sum of normalized area and normalized voltage (normalized to maximum possible area and voltage respectively). The amplitude of oscillation is very crucial and large amplitudes are required for better sensing capabilities. To achieve this, a fourth objective function: maximize displacement at resonance, is also implemented.

In our approach, the synthesis problem is translated into a constrained optimization formulation that is solved using a non-linear constrained optimization technique. During the optimization, designs are evaluated by the values of the constraint functions and the objective functions for the current values of the design variables. Depending on the choice of the objective function, there can be more than one minimum point in the optimization, due to the complex non-linear characteristics of the individual equations in the lumped-element models. Furthermore, since our goal is synthesis, we need to be independent of any choice of starting point for the optimization.

In order to increase the probability of finding a better design (i.e., move closer to the global optimum) a gridded multi-start algorithm coupled with a gradient-based constrained optimization (NPSOL) [19] efficiently solves for the global minimum of the objective function. The use of a starting grid eliminates the need to provide good starting points to the gradient-based optimization. The starting grid is formed by assigning 3 values to each design variable (as described in Section 3.1, there are 15 design variables) leading to  $3^{15}$  starting points. Each of these points in the design space is evaluated and 100 designs which best meet the constraints are selected. These 100 points are used as the starting points for the gradient-based optimization. A number of these 100

optimization runs may converge to the same design. From among the different designs resulting from these 100 optimization runs, the best design is chosen as the final synthesis result.

The non-linear constrained optimization formulation can be written as:

$$\begin{aligned}
 \min_{\underline{u}} \quad & z = \sum_{i=1}^k w_i \cdot f_i(\underline{u}) \\
 \text{s.t.} \quad & \underline{h}(\underline{u}) = 0 \\
 & \underline{g}(\underline{u}) \leq 0 \\
 & \underline{u} \in U_P
 \end{aligned}$$

where  $\underline{u}$  is the vector of independent design variables given in Table II;  $f_i(\underline{u})$  is a set of objective functions that codify performance specifications the designer wishes to optimize, *e.g.*, area;  $\underline{h}(\underline{u}) = 0$  and  $\underline{g}(\underline{u}) \leq 0$  are each a set of functions that implement the geometric and functional constraints given in Table III and Table IV. Scalar weights,  $w_i$ , balance competing objectives. The decision variables can be described as a set  $\underline{u} \in U_P$ , where  $U_P$  is the set of allowable values for  $\underline{u}$  (described by the bounds in Table II).

The MEMS design problem cannot be completely modeled in the non-linear constrained optimization formulation. Some of the design variables in the design (such as the number of comb fingers) are integer in nature. The number of comb fingers is initially treated as a continuous variable. When the optimization (called the RELAXED problem) terminates successfully, the number of comb fingers is truncated to the nearest integer and removed from the list of design variables. The optimization is run again (called the NON-RELAXED problem) with the result of the RELAXED problem as the starting point, resulting in the final synthesized design. Furthermore, all the geometry parameters will directly affect the physical microresonator layout. Therefore, they should be represented as integers with centi-micron units rather than as real numbers, as is the case in the classical non-linear constrained optimization formulation. To implement this the values of



the design variables that result from the NON-RELAXED problem are rounded off to the nearest centi-micron units.

### *3.4 Layout Generation*

Once the optimization results in a valid design, i.e., a set of values for the design variables, which satisfy all the requirements, these values are fed to a parameterized layout generation tool, CAMEL [1]. CAMEL produces a CIF file which contains the mask information required for fabrication of the synthesized microresonator. CAMEL was modified to produce simplified layouts of the microresonator so that the number of style variables is reduced.

### *3.5 Summary*

The synthesis tool has been described in detail. This tool is used to generate microresonator layouts for different frequencies and different design objectives. In the next chapter, we will detail the complex trade-offs involved in optimal design of microresonators, with the help of the synthesis results.

# Chapter 4. Synthesis Results and Synthesis Validation

The synthesis tool was used to generate layouts for 5 different frequencies for 4 different objective functions. For these microresonators, only the in-plane mode separation constraints described in Section 3.2.2, were imposed. The trends in the synthesis results with changing frequencies and objective functions are discussed. Out-of-plane mode separation constraints (also described in Section 3.2.2) are then included in the synthesis and the generated results are discussed. We evaluate the effectiveness of synthesis by comparing the predicted behavior of the synthesized microresonators with finite element analyses and through experimental measurements on fabricated microresonators.

## *4.1 Microresonator Layouts with In-plane Mode Separation Constraints*

Layouts were synthesized using 3, 10, 30, 100 and 300 kHz as the input frequency specification. These microresonators were synthesized for 4 different objective functions. The synthesis results are shown in Figure 10. As the frequency increases, we see that the overall size of the microresonator decreases. The length of the folded-flexure beams also becomes smaller at higher frequencies. Higher frequency microresonators need stiffer springs and lighter masses. Shorter beams are stiffer and smaller microresonators have lesser mass. Hence the observed trends in the size and the beam lengths.

The minimize-area microresonators are seen to be smaller than the other sets of microresonators. In some cases, the minimize-area microresonators have only one comb finger. The minimize-voltage microresonators have longer comb drives (because they have more comb fingers) than the other sets of microresonators. To produce adequate force with a small voltage, more comb fingers are required, since, the force produced is directly proportional to the number of comb fingers ((26)). The minimize-area and voltage microresonators are larger than the minimize-area microresonators and at the same time, have shorter comb drives than the minimize-voltage

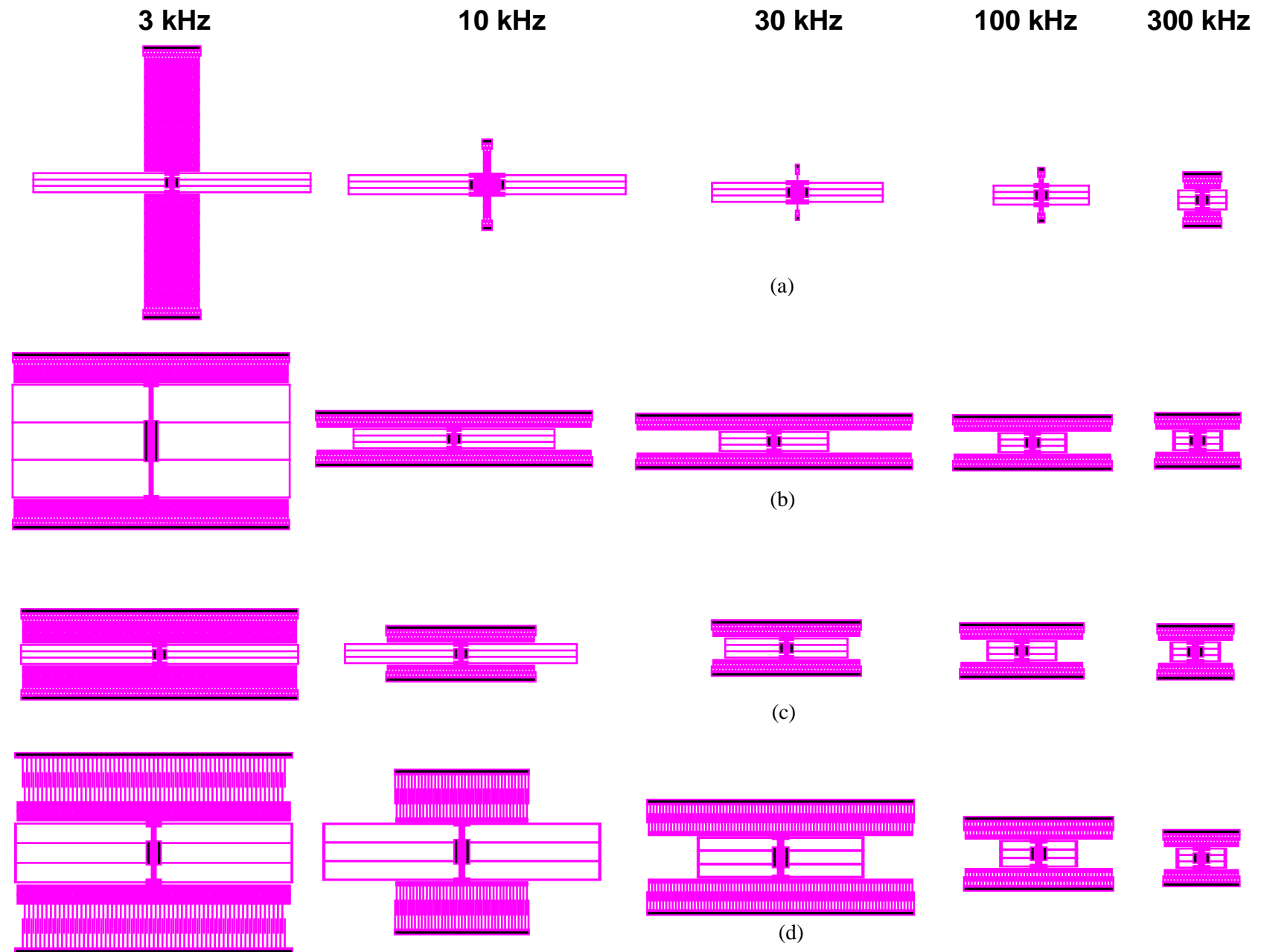


**FIGURE 10.** Layouts synthesized with in-plane mode separation constraints for 5 different frequencies and 4 different objective functions. (a) minimize area (b) minimize voltage (c) minimize area + voltage (d) maximize displacement at resonance

microresonators. The maximize-displacement microresonators have long comb fingers in order to accommodate the large motion amplitude of the shuttle during resonance.

#### 4.2 Frequency Limits on Synthesis

The synthesis tool cannot synthesize microresonators with frequencies smaller than 1.6 kHz or larger than 300 kHz. At the low frequency end, the plate masses have a large surface area. As seen in Figure 11, in the 1.6 kHz case the constraints on the overall size (700  $\mu\text{m}$  a side) are active.

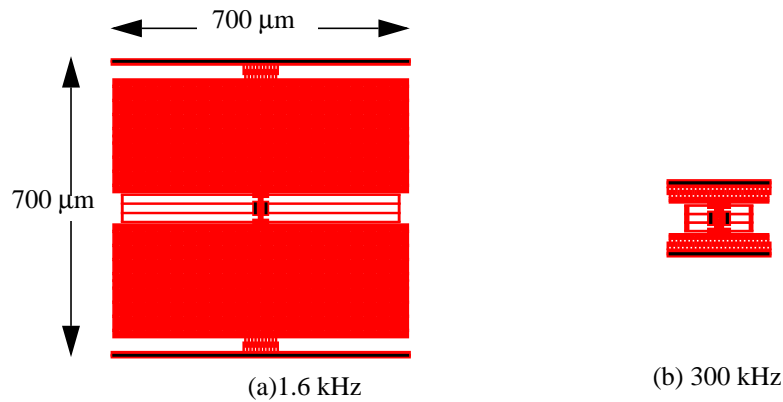


**FIGURE 11. Microresonators synthesized with the maximize displacement objective function. (a) 1.6 kHz, low frequency limit (b) 300 kHz, high frequency limit**

The larger area results in a large damping force and, therefore, a small quality factor. Therefore, it is difficult to maintain the quality factor to be greater than 5. Additionally, since the comb fingers are far away from the center of the shuttle mass, a small angular displacement can lead to a large instability torque. The synthesis tool is therefore not able to meet the quality factor constraint and the  $\theta_z$  instability constraint at frequencies lower than 1.6 kHz.

At the higher frequency end, the springs are very stiff in the y-direction. The central shuttle axle is therefore liable to bend if there is a y-directed force. The  $k_y$  accuracy constraint is, therefore, difficult to satisfy at frequencies higher than 300 kHz. To produce a displacement of 2  $\mu\text{m}$ , a larger force needs to be applied at 300 kHz than at lower frequencies, since the springs are stiffer at higher frequencies. Since the voltage that can be applied to the comb drives has an upper limit of

50 V, the only way to increase the force is by having more comb fingers. However, this increases the mass of the resonator and also the width of the comb drive. With an increased mass it is difficult to generate high-frequency resonators. Further, if the comb drive is too wide, the  $\theta_z$  mode separation constraint is difficult to meet. These are the constraints and trade-offs that determine the high-frequency limit on the synthesis for the MUMPS process design rules and the previously described minimum performance criteria.

#### *4.3 Microresonator Layouts with Out-of-plane Mode Separation Constraints*

Previously, we presented synthesized layouts which were optimized for different objective functions such as minimize microresonator area, minimize applied voltage, minimize a normalized sum of microresonator area and applied voltage, and maximize microresonator displacement at resonance. These resonators were fabricated in the MUMPS process [12]. All these devices are 2  $\mu\text{m}$  thick. Representative layouts are shown in Figure 12 (a) and (b). After the incorporation of the out-of-plane mode separation constraints in the synthesis tool, an attempt was made to synthesize layouts as before. However, it was found that the thickness of 2  $\mu\text{m}$  was not sufficient to meet these new constraints. With higher structural thickness, the springs will be stiffer in the out-of-plane modes and, therefore, these modes will have higher resonant frequencies. Hence, we introduced the structural thickness as a new design variable and implemented a new objective function: minimize a normalized sum of microresonator area, applied voltage and structural thickness. The layouts generated are shown in Figure 12(c). The thicknesses range from 3.7  $\mu\text{m}$  to 9.1  $\mu\text{m}$ . The mode separation constraints are more significant near the design corners, i.e., for the 300 kHz resonator. It is seen that the 300 kHz resonator in Figure 12 (b) has the least number of fingers and, therefore, has a smaller moment of inertia about the  $z$ -axis (pointing out of the plane of the paper). This is necessitated by the rotation-about- $z$  mode separation constraint. On the other hand, the 300 kHz resonator in Figure 12(c) has more comb fingers. However, since the design has a much thicker

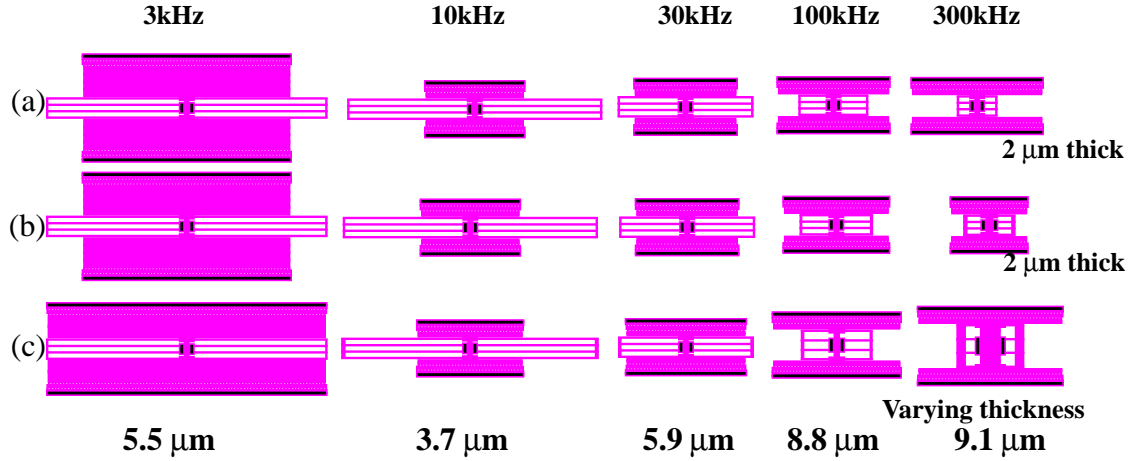


**FIGURE 12.** Comparison of layouts generated using increasing number of mode separation constraints for five frequencies. (a) 1 mode separation constraint (b) 3 in-plane mode separation constraints (c) 3 in-plane and 4 out-of-plane mode separation constraints. Layouts are optimized for area, voltage and thickness.

and wider truss beam, the mode separation constraint can still be met even though the moment of inertia is relatively large.

#### 4.4 Model Accuracy Verification with Finite Element Analyses (FEA)

The analytic expressions for spring constants and resonant frequencies were verified with FEA [20] using 3D 20-node quadratic brick elements to model the entire resonator structure. The important spring constants and corresponding resonant frequencies are shown in Figure 13. Analytic spring constants in  $x$  are within 10% of the FEA results (Figure 13(a)). Similarly, our frequency estimates in the  $x$  direction are also accurate to about 10%. The spring constants in the  $y$ -mode (Figure 13(c)) and the  $z$ -mode (Figure 13(b)) are accurate to about 20% at the lower frequencies, but are more than 30% off at 300 kHz. The  $\theta_z$  spring constant (Figure 13(c)) has errors of about 30%. In the two out-of-plane rotational modes (Figure 13(d) and (e)), the spring constant is accurate to about 2% at 3 kHz but is more than 50% off at 300 kHz. Predicted resonant frequencies of the  $z$ -mode are within 10% of the FEA results, while the resonant frequencies of the out-of-plane vibration modes are within 30% at lower frequencies, but are off by about 50% at 300 kHz. The flexure-mode and the in-plane rotation-mode resonant frequencies have a maximum error of 25%. (These values were obtained from a 2D FEA using 8-node quadratic plane-stress elements).

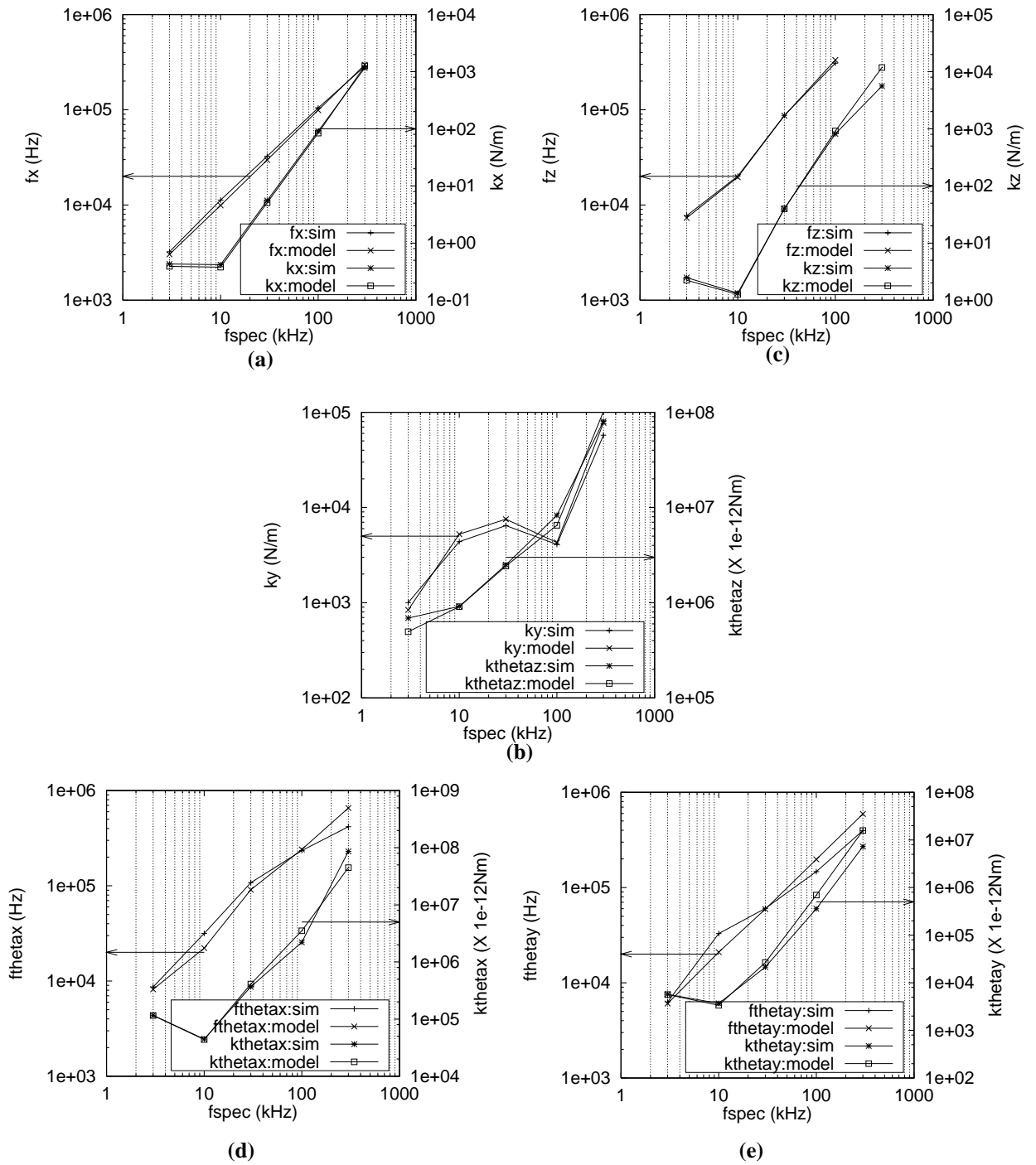


**FIGURE 13.** Comparison of predicted spring stiffness and resonant frequencies with finite element analysis for the microresonators shown in Figure 12(c). (a) spring constant and resonant frequency of the x-mode (b) spring constant and resonant frequency for the  $\theta_z$  mode (c) spring constant and resonant frequency for the z-mode (d) spring constant and resonant frequency for the  $\theta_x$  mode (e) spring constant and resonant frequency for the  $\theta_y$  mode.

Briefly stated, the x-mode is modeled to within 10% accuracy, while the other modes are about 20-30% off on an average.

In addition to calculating the spring stiffness and the resonant frequencies in the various modes, we also observed the dominant modes of oscillation of the microresonator. In particular, we observed the modes of two microresonators, both designed for 10 kHz, one (2  $\mu\text{m}$  thick) synthesized with the in-plane mode separation constraints while the other one (3.7  $\mu\text{m}$  thick) synthesized with out-of-plane constraints as well. The layouts of these are shown in the second column in Figure 12 (b) and (c) respectively. It is seen in Figure 14 that the 2  $\mu\text{m}$ -thick microresonator has two vibration modes which are lower than the x-mode, whereas, the 3.7  $\mu\text{m}$ -thick microresonator has the x-mode as the lowest mode, indicating that the mode separation constraints are effective.

#### 4.5 Experimental Verification

Resonators were fabricated in MUMPS, and the resonant frequencies and the quality factors of the x mode of vibration were measured.

The experimental setup to obtain the transfer function of the microresonator is shown in Figure 15. This setup uses Electromechanical Amplitude Modulation (EAM) [21]. The output is observed at the lower side-band frequency ( $f_c - f_d$ ). To get the transfer function,  $f_d$  is swept across

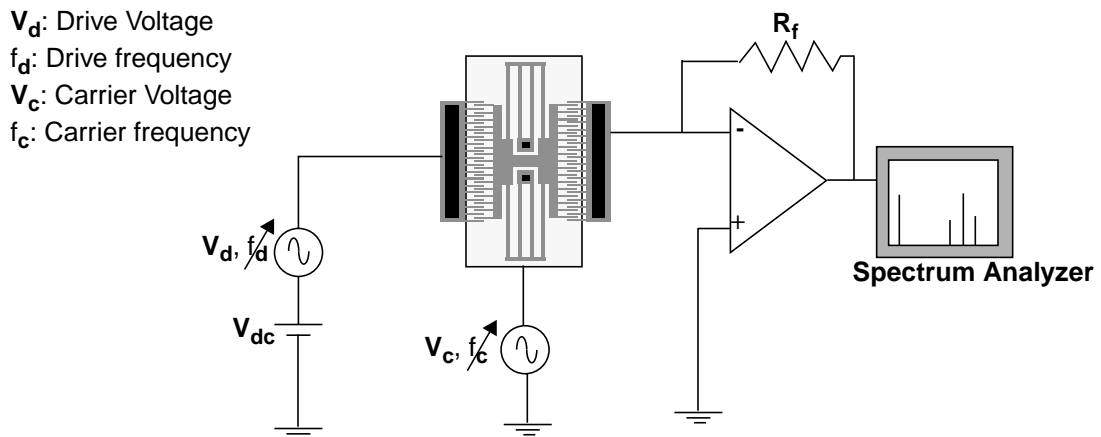


**FIGURE 15.** Setup for obtaining the transfer function of the microresonator employing Electromechanical Amplitude Modulation (EAM). One comb drive is used for actuation and the other for sensing. The sense current is passed through a transimpedance amplifier and the output spectrum is observed on a spectrum analyzer.



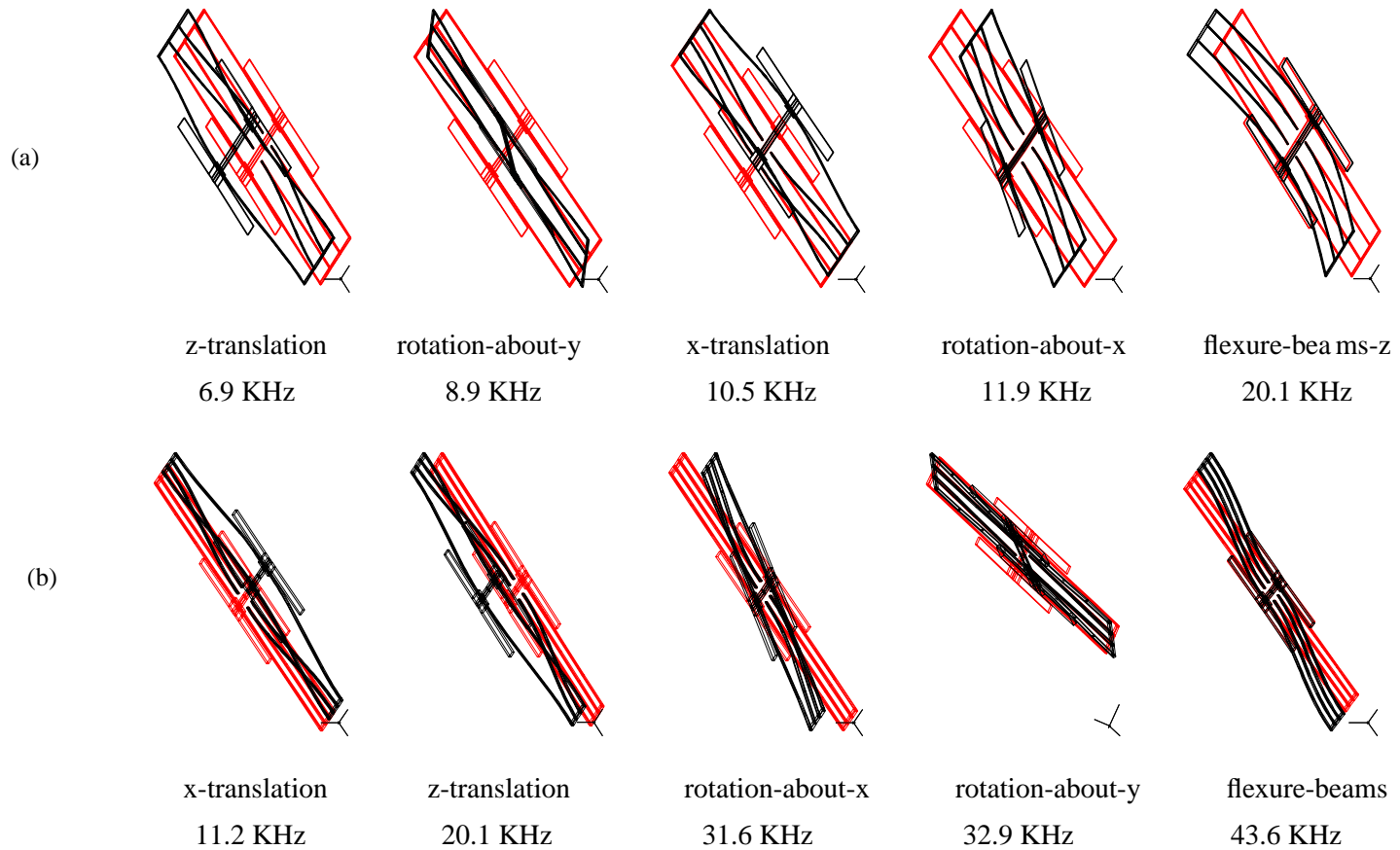


**FIGURE 14. Simulated vibration modes of two 10 KHz resonators. (a) Modes for the resonator synthesized with the in-plane mode separation constraints only. The dominant mode in this case is the z-translation mode at 6.9 KHz. (b) Modes for the resonator synthesized with the out-of-plane mode separation constraints as well. The thickness of this resonator is  $3.7\mu\text{m}$ . The dominant mode is the preferred x-translation mode and all the other vibration modes are well-separated from the dominant mode.**

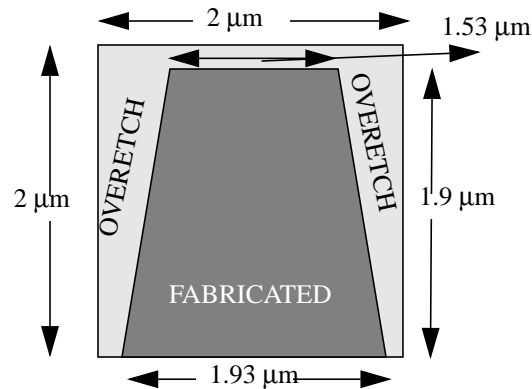


**FIGURE 16. Overetching of beams resulting in a trapezoidal cross-section as opposed to the expected rectangular cross-section**

the frequency range of interest and the output is observed. The carrier frequency,  $f_c$ , is also changed simultaneously so that the side-band frequency ( $f_c - f_d$ ) remains constant. The instruments used in the setup are controlled by a PC using HP-VEE scripts.

Comparison of the synthesized frequency and measured frequency of fabricated microresonators showed a consistent underestimation of about 70% of the desired frequency by the analytical equations in the synthesis system. A closer inspection of the fabricated microresonators showed a systematic  $0.07\mu\text{m}$  overetch of the structural layer at the bottom and  $0.47\mu\text{m}$  at the top surface (as shown in Figure 16, causing significant overestimation of the bending moment of inertia from the rectangular cross-section approximation, particularly for the thin  $2\mu\text{m}$  beams and trusses. Additionally, the measured value of structural film thickness was  $1.9\mu\text{m}$  instead of the nominal value of  $2\mu\text{m}$ .

The transfer functions obtained for 4 microresonators of specified frequency 10, 20, 30 and 100 kHz are shown in Figure 17. The measured resonant frequencies are about 30% lower than the specified frequency. For the 10 kHz resonator the measurements are riding on a background of about 40 dB, hence the vertical shift in the transfer function. From these measurements, the resonant frequency and the quality factor were extracted. These values are plotted in Figure 18 along with the values predicted by the models which included the beam overetch. Models for trapezoidal cross-section were incorporated in the synthesis tool and the synthesized designs were evaluated

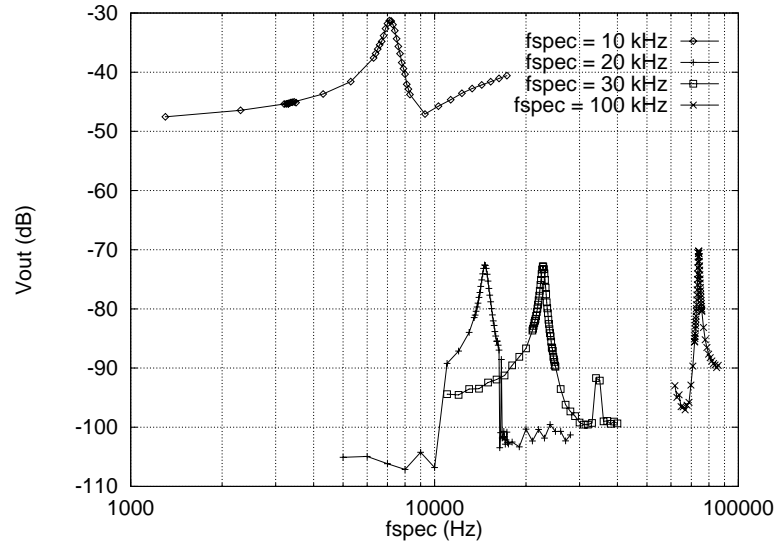


**FIGURE 17. Measured transfer functions for 4 different microresonators. The resonance peaks are clearly visible. However, the measurements become noisy as we move away from the resonant frequency**

taking measured over-etch parameters into account, for one-to-one verification with measured functional performance data. These analytical models are quite accurate. The measured resonant frequency matches to within 4% of the model. This implies that, if we were to have a process that has a well-characterized over-etch, we would be able to synthesize layouts whose performance will be exactly as expected.

The quality factor is accurate to about 20% at high frequencies (at 20 kHz, the model is accurate to within 5%). The quality factor model depends primarily on the damping models used. At higher frequencies, when the dimensions are small, the edge and finite-size damping effects

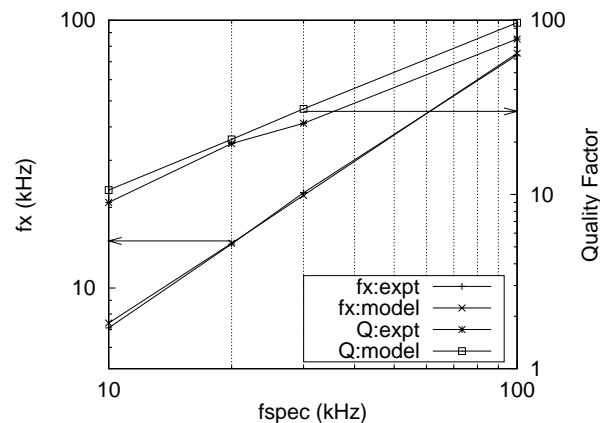


**FIGURE 18. Comparison of measurements of resonant frequency and quality factor with models.**

become more significant. Hence, we see more error in the quality factor model at higher frequencies.

#### *4.6 Summary*

Layouts synthesized for different objective functions and different specified frequencies suggest that the synthesis tool is functional. Performance predictions by the synthesis tool are verified by comparison with FEA. The effectiveness of the synthesis tool in implementing mode separation is also observed. Synthesized microresonators are fabricated and experimental measurements are made on them. In the next chapter, we draw conclusions from these comparisons and experimental measurements.

# Chapter 5. Summary, Conclusions and Future Work

## 5.1 Summary

The following tasks were completed during the course of this work.

1. Compiling models for the folded-flexure electrostatic comb drive microresonator. Specifically, this involved using and enhancing previously derived models for the spring constants and effective masses, damping force and the electrostatic comb drive force and deriving new models for the modes of vibration not modeled previously.
2. Building on the existing synthesis framework to develop a synthesis tool for the microresonator, formulating and encoding new constraints and objective functions to ensure better microresonators.
3. Synthesizing microresonator layouts from high-level specification using the synthesis tool for a range of frequencies and for different objective functions.
4. Examining the validity of the synthesis results and, if necessary, adding new constraints and improving models followed by re-synthesizing the layouts.
5. FEA of the synthesized microresonators to simulate the mechanical behavior of the microresonators. These analyses were used to determine if the models used were accurate throughout the range of the synthesis and if the assumptions made were justified.
6. Building a microresonator test setup using HP-VEE scripts to control the instruments and automatically obtain the microresonator transfer function. Resonant frequency and quality factor measurements were made on the fabricated microresonator using this setup.

## *5.2 Conclusions*

The synthesis tool can generate microresonator layouts from high-level specifications. The synthesized microresonators have resonant frequencies within 10% of the values predicted by the synthesis tool. The in-plane and out-of-plane mode separation constraints ensure that the other vibration modes are well-separated from the x-mode of vibration. The models for these modes are accurate to about 30%, but since the interest in these modes is only for maintaining sufficient separation in frequency from the x-mode, this is acceptable. With a well-characterized process, the synthesis tool can generate layouts which, when fabricated, match the predicted resonant frequencies and quality factors very well.

## *5.3 Future Work*

The synthesis work can be extended in a number of directions. Synthesis modules for other devices such as accelerometers and gyroscopes will be developed. This requires a dedicated modeling effort for each of these devices. Manufacturing variations need to be incorporated for accurate synthesis results.

In order to extend the synthesis methodology to any general MEM device without a dedicated modeling effort, the capability to generate models automatically is required. An adaptive macro-modeling algorithm, which uses the data from a number of FEA results to model the device accurately in a restricted range of the design space, can be embedded in the synthesis tool. Whenever the search for a good design wanders out of this range, the algorithm can be called again to generate new macromodels.

An alternative approach would be to have libraries of pre-compiled accurate models for standard MEMS components, like folded-flexure springs etc., and stitch these models together as dictated by the device topology and generate the models for the whole device. This will also facilitate synthesis at different levels: i.e., first at the device level which results in specifications for the components and then synthesis at the component level.

## References

- [1] *CaMEL Web Page*, <http://www.mcnc.org/camel.org>, MCNC MEMS Technology Applications Center, 3021 Cornwallis Road, Research Triangle Park, NC 27709.
- [2] N. R. Lo, E. C. Berg, S. R. Quakkelaar, J. N. Simon, M. Tachiki, H.-J. Lee, and K.S.J.Pister, "Parametrized layout synthesis, extraction, and SPICE simulation for MEMS," *Proc. ISCAS*, Atlanta, GA, 1996, pp. 481-484.
- [3] D. Haronian, "Maximizing microelectromechanical sensor and actuator sensitivity by optimizing geometry," *Sensors and Actuators A*, 50 (1995) 223-236.
- [4] G.K. Fedder and T. Mukherjee, "Physical Design For Surface-Micromachined MEMS," *Proc. 5th ACM/SIGDA Physical Design Workshop*, Reston, VA, April 1996, pp.53-60.
- [5] T. Mukherjee and G. K. Fedder, "Structured Design Of Microelectromechanical Systems," *Proceedings of the 34th Design Automation Conference (DAC '97)*, Anaheim, CA, June 9-13, 1997.
- [6] G.K. Fedder and T. Mukherjee, "Automated Optimal Synthesis of Microresonators," *Proc. 9th Intl. Conf. on Solid-State Sensors and Actuators (Transducers '97)*, Chicago, IL, June 16-19, 1997.
- [7] S. Iyer, T. Mukherjee and G. K. Fedder, "Multi-mode Sensitive Layout Synthesis of Microresonators," *Proceedings of the First International Conference on Modeling and Simulation of Microsystems, Semiconductors, Sensors and Actuators, (MSM '98)*, Santa Clara, CA, April 6-8, 1998
- [8] T. Mukherjee, S. Iyer and G. K. Fedder, "Optimization-based Synthesis of Microresonators," *Sensors and Actuators A*, To be published.
- [9] W. C. Tang, T.-C. H. Nguyen, M. W. Judy, and R. T. Howe, "Electrostatic Comb Drive of Lateral Polysilicon Resonators," *Sensors and Actuators A*, 21 (1990) 328-31.

- [10] C. T.-C. Nguyen and R. T. Howe, "Micromechanical resonators for frequency references and signal processing," *Proc. IEEE Int. Electron Devices Meeting*, San Francisco, CA, 1994, pp. 343.
- [11] M.-H. Kiang, O. Salgaard, K. Y. Lau and R. S. Muller, "Electrostatic Combdrive-Actuated Micromirrors for Laser-Beam Scanning and Positioning", *J. of Microelectromechanical Systems*, vol. 7, no. 1, March 1998, pp. 27-37.
- [12] D. A. Koester, R. Mahadevan, K. W. Markus, *Multi-User MEMS Processes (MUMPs) Introduction and Design Rules*, MCNC MEMS Technology Applications Center, 3021 Cornwallis Road, Research Triangle Park, NC 27709, rev. 3, Oct. 1994.
- [13] G. K. Fedder, *Simulation of Microelectromechanical Systems*, Ph.D. thesis, University of California at Berkeley, September 1994.
- [14] J. M. Gere and S. P. Timoshenko, *Mechanics of Materials*, 4th ed., Boston: PWS Publishing Co., 1997.
- [15] X. Zhang and W. C. Tang, "Viscous Air Damping in Laterally Driven Microresonators," *Sensors and Materials*, v. 7, no. 6, 1995, pp.415-430.
- [16] G. K. Fedder, Personal Communication
- [17] W. A. Johnson and L. K. Warne, "Electrophysics of Micromechanical Comb Actuators," *J. of Microelectromechanical Systems*, v.4, no.1, March 1995, pp.49-59.
- [18] C. H. Mastrangelo and C. H. Hsu, "A Simple Experimental Technique for the Measurement of the Work of Adhesion of Microstructures", *Technical Digest, IEEE Solid-State Sensor and Actuator Workshop*, Hilton Head Island, South Carolina, June 1992, pp. 208-212.
- [19] P. E. Gill, W. Murray, M. A. Saunders and M. H. Wright, *User's Guide for NPSOL (Version 4.0): A Fortran Package for Nonlinear Programming*, Technical Report SOL 86-2, Stanford University, January 1986.



- [20] *ABAQUS Web Page*, <http://www.hks.com>, Hibbitt, Karlsson, and Sorensen, Inc., 1080 Main Street, Pawtucket, RI 02860.
- [21] C. T-C. Nguyen, *Electromechanical Characterization of Microresonators for Circuit Applications*, MS thesis, University of California at Berkeley, April 1991.